

Look to Locate: Vision-Based Multisensory Navigation with 3-D Digital Maps for GNSS-Challenged Environments

Ola Elmaghraby[✉], Eslam Mounier[✉], *Graduate Student Member, IEEE*, Paulo Ricardo Marques de Araujo[✉], *Member, IEEE*, and Aboelmagd Noureldin[✉], *Senior Member, IEEE*

Abstract—In Global Navigation Satellite System (GNSS)-denied environments such as indoor parking structures or dense urban canyons, achieving accurate and robust vehicle positioning remains a significant challenge. This paper proposes a cost-effective, vision-based multi-sensor navigation system that integrates monocular depth estimation, semantic filtering, and visual map registration (VMR) with 3-D digital maps. Extensive testing in real-world indoor and outdoor driving scenarios demonstrates the effectiveness of the proposed system, achieving sub-meter accuracy 92% indoors and more than 80% outdoors, with consistent horizontal positioning and heading average root mean-square errors of approximately 0.98 m and 1.25°, respectively. Compared to the baselines examined, the proposed solution significantly reduced drift and improved robustness under various conditions, achieving positioning accuracy improvements of approximately 88% on average. This work highlights the potential of cost-effective monocular vision systems combined with 3D maps for scalable, GNSS-independent navigation in land vehicles.

Index Terms—Navigation, Positioning, Autonomous Driving, Computer Vision, Map Registration, Monocular Cameras.

I. INTRODUCTION

POSITIONING is a cornerstone of autonomous driving, enabling vehicles to plan, control, and make decisions [1]. While global navigation satellite system (GNSS) technologies provide high accuracy positioning capabilities in open-sky environments [2], they become unreliable or even denied in environments such as dense urban areas, tunnels, and underground parking [3]. To compensate for GNSS limitations, some approaches employ high-resolution light detection and ranging (LiDAR)-based positioning systems [4] or integrate high-grade inertial navigation system (INS) [5]. Although these solutions can provide accurate and reliable positioning, their high cost hinders their practicality for consumer-level deployment.

In contrast, cameras offer a cost-effective, lightweight, and widely available sensing modality. They are already integrated in most modern vehicles, such as dashcams and advanced

This research is supported by grants from the Natural Sciences and Engineering Research Council of Canada (NSERC) under grant numbers: RGPIN-2020-03900 and ALLRP-560898-20. (*Corresponding author: Ola Elmaghraby.*)

Ola Elmaghraby and Paulo de Araujo are with the Department of Electrical and Computer Engineering, Queen's University, Kingston, ON K7L 3N6, Canada (e-mail: ola.elmaghraby.a@queensu.ca; paulo.araujo@queensu.ca).

Eslam Mounier is with the Department of Electrical and Computer Engineering, Queen's University, Kingston, ON K7L 3N6, Canada, and also with the Department of Computer and Systems Engineering, Ain Shams University, Cairo 11535, Egypt (e-mail:eslam.abdelmoneem@queensu.ca).

Aboelmagd Noureldin is with the Department of Electrical and Computer Engineering, Royal Military College of Canada, Kingston, ON K7K 7B4, Canada, and also with the School of Computing, Queen's University, Kingston, ON K7L 2N8, Canada, (e-mail:aboelmagd.noureldin@rmc.ca).

driver-assistance systems (ADAS) systems, and provide rich visual information useful for navigation and perception [6]. Among camera-based systems, monocular setups are particularly attractive due to their simplicity and minimal hardware requirements.

However, they face inherent challenges such as scale ambiguity, accumulated drift, and sensitivity to lighting variations or dynamic scenes [7]. Recent advances in deep learning (DL), especially in monocular depth estimation, have enabled the extraction of metric-scale 3-D structure from single images [8]. This capability paves the way for the innovative use of monocular cameras in applications such as simultaneous localization and mapping (SLAM) and map-based navigation.

In parallel, the increasing availability of high-definition (HD) and 3-D digital maps, when combined with perception sensors, opens new avenues for achieving high-accuracy map-based positioning [9]. Specifically, by aligning camera-derived 3-D information to pre-existing maps, a globally consistent navigation solution can be achieved. These DL-based developments establish monocular solutions as a promising cost-effective alternative to robust positioning, particularly in GNSS-challenged environments.

Building on these observations, this work addresses the challenge of achieving cost-effective, accurate, and drift-free positioning in GNSS-challenged environments through the development of a vision-based map alignment positioning solution. The paper specifically focuses on the integration of monocular depth estimation with pre-existing 3-D maps to obtain absolute pose corrections integrated within an error-state extended Kalman filter (ES-EKF) framework.

The contributions of this work are as follows:

- 1) Introducing a DL-based monocular 3-D point cloud generation pipeline, integrating a state-of-the-art depth estimation model enhanced by depth preprocessing and postprocessing, semantic and transient object removal (STOR), and point cloud refinement.
- 2) Proposing a novel visual map registration (VMR) pipeline that uniquely registers the generated monocular point cloud to the 3-D digital maps, initialized using prior pose information, to provide accurate pose corrections.
- 3) Developing an ES-EKF-based fusion framework that integrates the on-board motion sensors (OBMS) data with VMR output to produce a smooth positioning solution with reduced drift.
- 4) Validating the effectiveness of the proposed multi-sensor system through real-world driving tests conducted in both urban and indoor environments.

The remainder of this paper is organized as follows. Section II reviews related work. Section III provides an overview of the proposed system. Section IV describes the monocular 3-D point cloud generation pipeline, while Section V introduces the vision-to-map registration pipeline for positioning. Section VI presents the multi-sensor fusion strategy. Section VII outlines the experimental setup, and Section VIII reports the results. Finally, Section IX concludes the paper.

II. RELATED WORK

A. Vision-Based Dead Reckoning and Sensor Fusion

Vision-based navigation systems leverage camera inputs to estimate a vehicle’s pose (position and orientation) and understand its environment [10]. Two foundational approaches in this domain are visual odometry (VO) [11] and SLAM [12]. In the context of this work, the term SLAM is used to specifically refer to visual simultaneous localization and mapping (VSLAM) for simplicity. Both methods operate by detecting, describing, and matching visual features across image sequences to estimate motion and structure. However, these methods suffer from drift, scale ambiguity (particularly for monocular cameras), and, in the case of SLAM, strong reliance on loop closure [13]

To address such challenges, many recent works fuse monocular vision with complementary sensors like inertial measurement unit (IMU), wheel odometry from on-board diagnostics II (OBDII) data, and LiDAR. Optimization-based visual-inertial odometry (VIO) systems such as Visual-Inertial Systems (VINS) [14] have proven effective on drones. [15] developed a visual-inertial-wheel odometry (VIWO) model and a novel data-driven DL method to model and mitigate slippage-induced errors effectively. VA-LOAM [16] uses LiDAR as the primary sensor for SLAM, enhancing visual feature matching. Other works use factor-graph optimization to integrate cameras, LiDAR, and IMU [17], or semantic-enhanced SLAM [18] for robust positioning under varying conditions.

Although VO and SLAM systems enhanced with sensor fusion significantly improve motion estimation accuracy and robustness, they still primarily provide relative pose estimates unless anchored to known global maps or fused with absolute sensors. Additionally, a monocular camera cannot directly measure absolute scale or depth, and visual methods can falter under poor lighting or repetitive textures [7]. This has led to numerous works aimed at improving monocular visual navigation via novel depth estimation techniques and map-based positioning.

B. Monocular Depth Estimation for Metric Scale

DL has enabled significant advances in estimating depth from a single image. Early lightweight models such as Fast-Depth [19] achieved real-time inference on embedded devices. Monodepth2 [20] introduced self-supervised training but was limited to relative depth due to scale ambiguity.

To address this, geometric constraints were incorporated. MonoPP [21] leveraged planar-parallax geometry and fixed camera setups to recover metric scale. Foundation models such

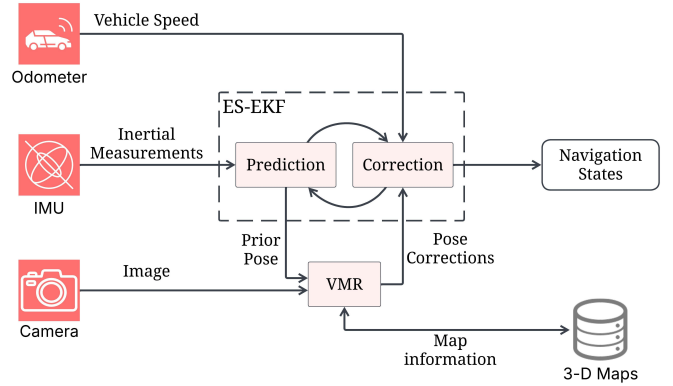


Fig. 1. Overview of System Components.

as Depth Anything [22] and ZoeDepth [23] combined large-scale pretraining with fine-tuning for robust, generalizable depth estimation.

Metric3D [8], [24] addressed scale variation and dataset bias by introducing a canonical camera transform and training on over 8 million images, achieving accurate metric predictions even under mixed-camera conditions.

Due to these advances, the performance gap between stereo and monocular systems has significantly narrowed. While stereo provides triangulated depth, it requires precise calibration, synchronization, and a suitable baseline—which can be limiting in embedded or automotive applications. In contrast, monocular systems are lighter, cheaper, and easier to deploy.

C. Map-Based positioning

There is a growing industrial shift toward map-based positioning in automotive applications [25]. HD maps and semantic vector maps are now used in many modern ADAS and autonomous vehicle stacks. These maps enable absolute positioning by aligning live sensor data—typically camera or LiDAR—with prior environmental representations [26], [27].

Indoor environments (e.g., warehouses, parking garages) lack GNSS entirely. Solutions like Lopes *et al.* [28] align vision-derived free-space maps with 2-D floorplans, while radio detection and ranging (RADAR)-based systems [29] operate in visually degraded settings.

In outdoor urban driving, visual cues from stable man-made structures enable map-based positioning. Yu *et al.* [30] and Zhao *et al.* [31] demonstrate efficient positioning by matching monocular images to vector maps.

Cross-modal alignment between 2-D vision and 3-D maps remains an active area. Learning-based methods like I2D-Loc [32] refine initial pose estimates via image-to-LiDAR alignment, while newer works like FreeReg [33] use pretrained diffusion models for modality-agnostic descriptors.

III. SYSTEM OVERVIEW

The proposed system integrates monocular vision, inertial sensing, and vehicle odometry within an ES-EKF positioning framework to enable resilient and accurate vehicle positioning in GNSS-challenged environments. For simplicity, we refer

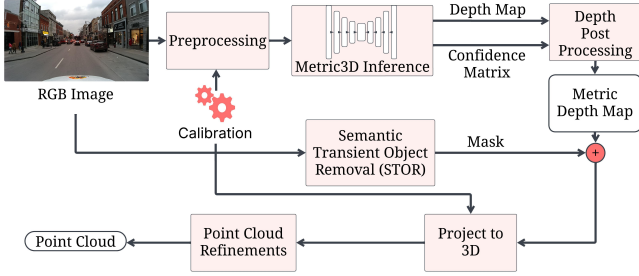


Fig. 2. Overview of the point cloud generation process, from depth estimation to filtering.

to the ES-EKF as extended Kalman filter (EKF) throughout the remainder of this paper. An overview of the system architecture is illustrated in Fig. 1.

Monocular images are processed using a DL-based pipeline to generate dense 3-D point clouds with metric depth. These point clouds are refined and then aligned with a 3-D reference map through VMR, which employs the generalized iterative closest point (GICP) algorithm to compute absolute pose corrections, helping to diminish long-term drift. Simultaneously, inertial measurements from the IMU are propagated through an INS algorithm within the prediction step of the EKF. Velocity measurements from the OBDII interface are used to constrain velocity drifts. The EKF continuously integrates these multi-modal measurements to maintain robust estimates of the navigation states. The latest EKF estimates are fed back into the VMR pipeline to guide subsequent registration steps and into the INS algorithm to reset state errors, forming a closed-loop system.

IV. DEEP LEARNING-BASED MONOCULAR 3-D POINT CLOUD GENERATION PIPELINE

This work presents a structured pipeline to generate 3-D point clouds from monocular images, as presented in Fig. 2. The pipeline begins with the depth estimation using a single image and a DL-based model. The obtained depth map is then post-processed to remove dynamic objects and correct structural inconsistencies. Finally, the processed depth map is projected onto a 3-D space to generate a point cloud, which is further refined to enhance its quality and reduce computational complexity. All the steps are detailed in the following sections.

A. Preprocessing

The input red green blue (RGB) image is first undistorted using the camera’s intrinsic matrix \mathbf{K} and distortion coefficients. The rectified image is resized to a fixed resolution of 616×1064 , maintaining the aspect ratio through symmetric padding with the mean values of the dataset, μ . Channel-wise normalization is then applied using the mean and standard deviation (μ, σ) , following standard image preprocessing practices for pretrained DL models [34]. These preprocessing steps ensure scale-invariant inputs suitable for Metric3Dv2’s zero-shot metric depth and surface normal estimation.

B. Depth Estimation Using Metric3D

The second step in the point cloud generation pipeline involves estimating depth from monocular images. Depth estimation is performed using the Metric3D model [8], [24], a monocular depth estimation framework that uses DL to infer metric-scale depth maps from single RGB images. To address the challenge of metric depth ambiguity caused by varying camera parameters, particularly focal length, all training data were transformed into a canonical camera space, where images are treated as if captured by a standard camera. This is done either by rescaling depth labels or by resizing input images, effectively normalizing focal length differences. This approach allows the model to learn consistent metric depth across diverse cameras without embedding camera intrinsics in the network.

Metric3D has shown strong performance on standard benchmarks such as KITTI and datasets, outperforming many existing depth estimation models [8]. The effectiveness of the model was demonstrated in terms of addressing scale ambiguity and producing accurate metric depth from monocular images. However, additional processing steps are required to refine the depth information and improve geometric consistency for downstream applications.

C. Depth Post Processing

Metric3D produces two primary outputs: the predicted depth map and a corresponding confidence matrix that assigns a confidence score to each pixel ranging from 0 to 1. Low-confidence regions were observed in areas corresponding to the sky and distant in small edges. To mitigate the influence of unreliable predictions, a confidence threshold of 0.75 was applied, removing depth values associated with confidence scores below this threshold.

Additionally, since Metric3D generates predictions in a canonical space, a transformation is required to map the predicted depth back to the camera coordinate system. This transformation is performed using the following scaling relation:

$$\mathbf{D}_{\text{metric}} = \mathbf{D}_{\text{pred}} \times \frac{f_{\text{input}}}{f_{\text{canon}}}, \quad (1)$$

where \mathbf{D}_{pred} is the raw depth prediction from Metric3D, f_{canon} is the training canonical focal length and f_{input} is the focal length of the input image. The resulting $\mathbf{D}_{\text{metric}}$ represents the corrected, camera-consistent metric depth map used in subsequent stages.

D. Semantic Transient Object Removal (STOR)

Dynamic and transient objects, such as vehicles, pedestrians, and buses, introduce inconsistencies between the generated point cloud and the static reference map [35], particularly in indoor environments where such objects are absent or appear in different locations. These mismatches can cause significant misalignment during the registration process. To mitigate this, we implement a semantic filtering step that removes such objects from the depth map prior to point cloud generation.

This method leverages a pre-trained DL instance segmentation model, specifically Mask region-based convolutional

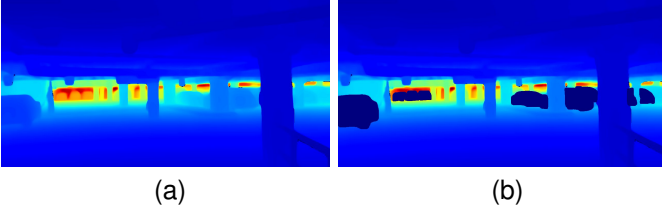


Fig. 3. Demonstration of the effect of the STOR stage. (a) Before filtering. (b) After filtering, the transient objects are dark, indicating 0 depth.

neural network (R-CNN) from the Detectron2 framework [36]. This model was chosen for its high accuracy and robustness in detecting and providing pixel-level segmentation masks for objects in complex urban environments, as a result of training on large-scale datasets such as common objects in context (COCO).

The model is applied to the RGB image to detect and segment different objects, including pedestrians, bicycles, cars, motorcycles, buses, trains, and trucks. After the segmentation masks have been obtained, a dilation filter is applied to the masks to account for potential inaccuracies at the boundaries of the detected objects. The dilation operation expands the mask regions by a predefined kernel size of $(7, 7)$, ensuring that any distortions or artifacts around the edges of the objects are included in the mask. The refined segmentation masks are then applied to the depth map to remove the regions corresponding to the objects as presented in Fig. 3. This is achieved by setting the depth values of the masked regions to zero, effectively excluding these areas from the point cloud generation process.

E. Project to 3-D

The next step is to generate the point cloud from the processed depth map by: projecting depth values into the 3-D camera frame, aligning the result with the body frame, and applying downsampling to reduce complexity.

1) *Projection from 2-D Image Plane to 3-D Camera Frame:* Each pixel (u, v) of the depth map, with its corresponding corrected depth d , is projected into the 3-D camera frame using the pinhole camera model, resulting in a 3-D point cloud as illustrated in Fig. 4b. The intrinsic parameters of the camera, including the focal lengths f_x and f_y and the principal point (c_x, c_y) , are used to compute the 3-D coordinates in the camera frame, (X_c, Y_c, Z_c) , as follows:

$$X_c = \frac{(u - c_x) \cdot d}{f_x}, \quad Y_c = \frac{(v - c_y) \cdot d}{f_y}, \quad Z_c = d. \quad (2)$$

2) *Transformation to the Body Frame:* The 3-D points in the camera frame are transformed to the body frame using the extrinsic calibration parameters, which describe the relative pose between the camera and the body frame. This rigid transformation is defined by a rotation matrix $\mathbf{R}_{\text{calib}} \in SO(3)$ and a translation vector $\mathbf{t}_{\text{calib}} \in \mathbb{R}^3$ that are obtained from the

calibration process. The 3-D coordinates in the body frame, (X_b, Y_b, Z_b) , are computed as:

$$\begin{bmatrix} X_b \\ Y_b \\ Z_b \end{bmatrix} = \mathbf{R}_{\text{calib}} \begin{bmatrix} X_c \\ Y_c \\ Z_c \end{bmatrix} + \mathbf{t}_{\text{calib}}, \quad (3)$$

3) *Voxel Grid Downsampling:* To reduce computational complexity and storage requirements, a voxel grid downsampling filter is applied to the transformed point cloud. The space was divided into voxels of size 0.2 m. Each voxel aggregates points within its bounds and approximates them with their centroid. This process preserves the overall structure of the point cloud while significantly reducing the number of points.

F. Point Cloud Refinements

Despite significant advances in monocular depth estimation DL-based models, the resulting point clouds often contain geometric inconsistencies due to prediction uncertainty at long distances, scene artifacts and depth noise around fine structures. To improve registration accuracy and computational efficiency, the point cloud undergoes a three-stage refinement process.

1) *Point Cloud Cropping:* Monocular depth estimation is known as an ill-posed task [37], where objects in a 2-D image often lack sufficient information to accurately estimate depth. This limitation becomes more pronounced as the distance from the object increases, making it challenging to infer a precise metric depth [38].

To mitigate the increasing uncertainty in depth estimates with distance, a depth cropping step is applied to exclude points beyond a specified range. Additionally, in indoor environments, ceiling regions often exhibit geometric deformations, e.g., pipes and cable trays, that compromise accuracy. Therefore, points above a height threshold are also removed to suppress ceiling artifacts. The filtered point cloud $\mathcal{P}_{\text{crop}}$ is obtained by:

$$\mathcal{P}_{\text{crop}} = \{\mathbf{p} \in \mathcal{P} \mid d(\mathbf{p}) < d_{\text{max}}, h(\mathbf{p}) < h_{\text{max}}\}, \quad (4)$$

where $d(\mathbf{p})$ is the depth of the point \mathbf{p} , $h(\mathbf{p})$ is its height, and d_{max} , h_{max} are the predefined depth and height thresholds, respectively. An output example is illustrated in Fig. 4c.

2) *Scale Correction:* Although the point cloud is on the metric scale, a slight scale inconsistency was observed. Empirical evaluation revealed a consistent scale factor, which was quantified by aligning a subset of generated point clouds with their corresponding scans from LiDAR using the iterative closest point (ICP) algorithm [39]. The LiDAR scans serve as ground truth references because of their high accuracy and metric consistency. The estimated scale factor, denoted $s \in \mathbb{R}^+$, was then uniformly applied to all point clouds on all trajectories tested. The scaled point cloud $\mathcal{P}_{\text{scale}}$ is computed as:

$$\mathcal{P}_{\text{scale}} = \{\mathbf{p}' = s \cdot \mathbf{p} \mid \mathbf{p} \in \mathcal{P}_{\text{crop}}\}, \quad (5)$$

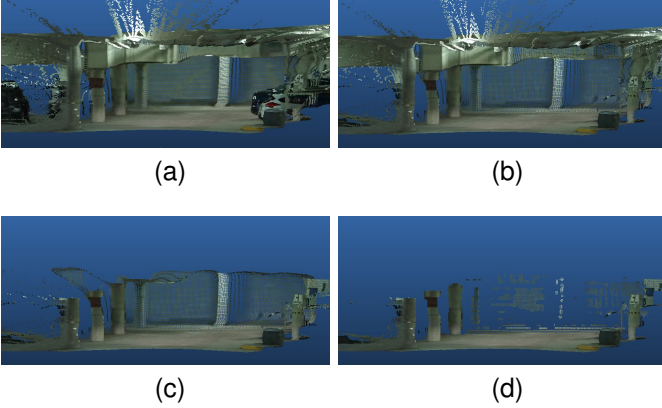


Fig. 4. Point Cloud pipeline output. (a) Original Point Cloud. (b) After STOR. (c) After cropping. (d) After filtering

3) *Statistical Outlier Removal*: Although the depth prediction model produces consistent results, it interpolates depth values across region boundaries, reducing edge sharpness, particularly for thin structures such as traffic lights, street poles, and parking garage pillars. When projected into 3-D space, this interpolation introduces distorted “tails” or elongated artifacts that degrade point cloud quality.

To mitigate these issues, as shown in Fig. 4d, a statistical outlier removal (SOR) algorithm is applied. For every point \mathbf{p}_i , the mean distance μ_i from its k nearest neighbors is computed. Points that deviate significantly from the global distribution are removed as:

$$\mathcal{P}' = \{\mathbf{p}_i \in \mathcal{P}_{\text{scale}} \mid \mu_i \leq \mu + \tau \cdot \sigma\}, \quad (6)$$

where \mathcal{P}' is the output filtered cloud, μ and σ are the global mean and standard deviation of the μ_i values across all points.

In practice, most of the noise is removed using an initial SOR pass with conservative parameters ($k = 6$, $\tau = 1.0$). However, residual artifacts, particularly in regions with strong depth discontinuities, require a second filtering step with more relaxed settings ($k = 10$, $\tau = 2.0$) to effectively eliminate subtle outliers.

V. VISUAL MAP REGISTRATION (VMR)

Point cloud registration is used to align the generated point cloud with a reference map to compute absolute pose corrections. These corrections are then fused within the EKF framework to mitigate drift and improve long-term accuracy. Before registration, the final output of the point cloud generation step \mathcal{P}' in the body frame is transformed into the local-level frame using the a priori pose estimate from the EKF as:

$$\tilde{\mathcal{P}} = \{\mathbf{T}^- \mathbf{p}' \mid \mathbf{p}' \in \mathcal{P}'\}, \quad (7)$$

where

$$\mathbf{T}^- = \begin{bmatrix} \mathbf{R}^- & \mathbf{t}^- \\ \mathbf{0} & 1 \end{bmatrix},$$

where $\mathbf{T}^- \in SE(3)$ is the transformation matrix from the EKF a priori pose estimate, and $\tilde{\mathcal{P}}$ is the point cloud in the local-level frame.

TABLE I
COMPARISON OF GROUND AND SURROUNDING POINT COUNTS FOR INDOOR AND OUTDOOR ENVIRONMENTS.

Environment	Ground Points	Surrounding Points
Indoor	180,695	39,599
Outdoor	324,537	405,677

The registration process differs between indoor and outdoor environments due to variations in structure and feature distribution. However, both rely on the GICP algorithm as the core of the alignment process. An overview of the registration workflow for both environments is illustrated in Fig. 5.

A. GICP Algorithm

The registration was performed using the GICP algorithm, which extends the standard ICP algorithm by modeling local surface geometry and incorporating uncertainty in the point cloud data through per-point covariance estimates [40]. This extension makes it particularly well-suited for aligning point clouds with varying densities and structures and offers more robustness to noise and outliers compared to the point-to-point and point-to-plane ICP variants.

GICP estimates a rigid transformation $\Delta \mathbf{T} \in SE(3)$ that aligns the source point cloud, generated from the monocular pipeline, to the target point cloud from the reference 3-D map. This transformation is then applied to the EKF prior pose estimate \mathbf{T}^- to obtain the corrected pose $\hat{\mathbf{T}}$ as:

$$\hat{\mathbf{T}} = \Delta \mathbf{T} \mathbf{T}^-. \quad (8)$$

B. Indoor Registration

Indoor environments, such as parking garages, possess distinct structural features, including floors, walls, pillars, and ceilings, which require additional measures to effectively adapt to and leverage the characteristics of the setting.

1) *Point Cloud Splitting*: In indoor environments, after the transient objects are removed, the point cloud is dominated by ground points, with fewer points corresponding to the pillars and walls. This imbalance can bias the registration process, causing it to optimize primarily for the ground while neglecting vertical features. To address this, a splitting algorithm was applied to separate the ground points from the surrounding points (e.g., pillars and walls). As illustrated in TABLE I, the average number of ground points in indoor environments far exceeds the average number of surrounding points (after cropping ceiling points) based on a tested trajectory, whereas outdoor environments exhibit a more balanced distribution.

To further enhance registration quality, a 2-D projection of the surrounding point cloud and the indoor map was applied. This projection was generated from a top-down view, condensing the vertical features (e.g., pillars and walls) into a 2-D plane. The ground points were removed from both the point cloud and the map before projection to focus on the vertical structures. This approach improved the robustness of the registration by emphasizing the dominant vertical features in indoor environments.

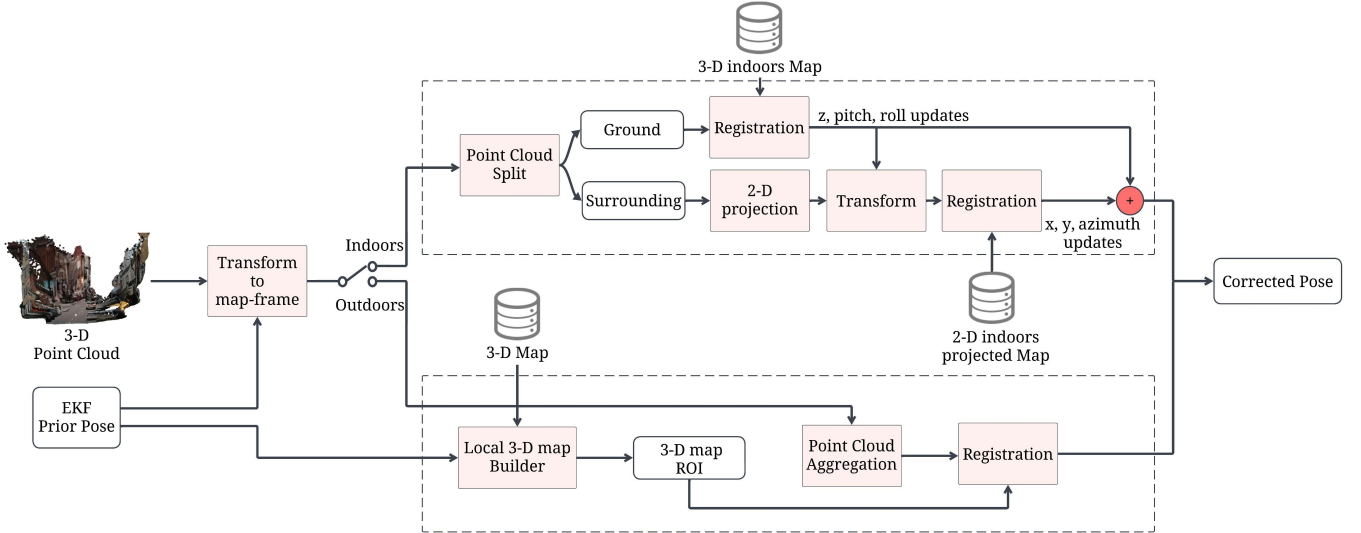


Fig. 5. Overview of the indoor and outdoor point cloud registration process.

2) *Two Stage Registration*: The registration process is performed in two stages to incrementally refine the alignment of the estimated trajectory. In the first stage, known as ground registration, the ground point cloud is aligned to correct for errors in the vertical z -axis as well as the pitch (θ) and roll (ϕ) angles.

The resulting GICP transformation matrix is then decomposed into its Euler angles and translation components. A new transformation matrix $\Delta\mathbf{T}_v$ is reconstructed using only the correction vertical components (Δz , $\Delta\theta$, and $\Delta\phi$) and applied to the surrounding point cloud following (7).

Next, the vertically aligned surrounding point cloud is registered to the corresponding portion of the map. This step focuses on refining the components of the horizontal position x and y , along with the azimuth (ψ) angle. The GICP output is used to construct a transformation matrix $\Delta\mathbf{T}_h$ using horizontal corrections (Δx , Δy , and $\Delta\psi$) to improve the horizontal alignment without overriding the ground corrections applied earlier.

Finally, the transformations obtained from both registration stages are integrated as:

$$\Delta\mathbf{T} = \Delta\mathbf{T}_h \Delta\mathbf{T}_v, \quad (9)$$

which is then applied to the EKF prior pose estimate after (8). The resulting corrected pose $\hat{\mathbf{T}}$ is fused into the EKF to improve the overall trajectory estimation.

C. Outdoor Registration

Outdoor trajectories are generally free of spatial constraints, and the corresponding 3-D maps can cover large areas. To efficiently manage this, the outdoor maps in this work are organized into a geospatial database structure, as described in Section VII-B. For each registration epoch, a local subset of the map is retrieved based on the vehicle's current position. Following the approach in [41], a region of interest (ROI) map of size 100×100 meters is centered on the latest EKF position estimate. This ROI is assembled by querying

the offline geospatial database, which stores pre-aligned 3-D .las files containing high-resolution and georeferenced LiDAR scans of the environment. The resulting ROI map, denoted as \mathcal{P}_{ref} , serves as reference for the alignment process.

Unlike indoor environments, outdoor scenes typically exhibit a more balanced distribution of features across ground and vertical structures (e.g., buildings, trees, signs). Additionally, since the ceiling is cropped in indoor environments, the depth threshold used for cropping in outdoor settings is higher than that in indoor scenarios, affecting the number of points, as illustrated in TABLE I. As a result, the point cloud splitting step is not required. However, due to the generally larger depth ranges encountered outdoors, monocular depth estimation tends to suffer from an increased error at longer distances, as discussed in Section IV-F1. To mitigate this, we aggregate point clouds across multiple frames based on displacement. This aggregation helps smooth out local depth estimation errors.

The aggregation process starts with an empty point cloud buffer and monitors vehicle displacement using the EKF trajectory. When the displacement from the last aggregation position exceeds a certain threshold d_{min} , it is transformed into the world frame using the corresponding EKF pose, following (7), and its points are added to the point cloud buffer. Aggregation continues until the total distance traveled exceeds a threshold d_{max} , after which the buffer points are merged, yielding a point cloud denoted as $\mathcal{P}_{\text{merged}}$. Then, voxel grid filtering is applied to downsample the aggregated point cloud.

A full 3-D GICP registration is then performed to align the aggregated source point cloud $\mathcal{P}_{\text{merged}}$ with the target reference map \mathcal{P}_{ref} , yielding the correction transformation matrix $\Delta\mathbf{T}$. The updated pose matrix $\hat{\mathbf{T}}$ is obtained following (8), which corrects all six pose states (x , y , z , θ , ϕ , ψ), and is subsequently incorporated into the EKF correction step.

VI. MULTI SENSOR FUSION

The proposed sensor fusion framework integrates measurements from onboard sensors, including an IMU and vehicle speed via OBDII, along with corrections from the visual map registration (VMR) module, to estimate the pose of a land vehicle. While all sensor measurements are acquired in the body frame, state estimation is performed in the local east-north-up (ENU) navigation frame. The fusion relies on an EKF, where the nominal state is propagated using INS mechanization, and external measurements provide corrections to position, velocity, and orientation.

A. Inertial Navigation Systems (INS) Mechanization

The INS estimates the position, velocity, and orientation of a moving platform by integrating inertial measurements from the IMU [42]. The system state consists of orientation $\mathbf{R}_k \in \text{SO}(3)$, velocity $\mathbf{v}_k \in \mathbb{R}^3$, and position $\mathbf{p}_k \in \mathbb{R}^3$, all expressed in the local ENU navigation frame.

The measured linear acceleration \mathbf{f}_{k-1} and the angular velocity $\boldsymbol{\omega}_{k-1}$ are first corrected by their respective biases $\mathbf{b}_{f,k-1}$ and $\mathbf{b}_{\omega,k-1}$. Orientation is updated using a quaternion-based integration of the corrected angular increment. The resulting orientation \mathbf{R}_k is used to transform the corrected acceleration from the body frame to the navigation frame. The velocity and position are then updated using first- and second-order integration, respectively:

$$\mathbf{R}_k = \mathbf{R}_{k-1} \otimes \text{quat}\left(\frac{1}{2}(\boldsymbol{\omega}_{k-1} - \mathbf{b}_{\omega,k-1})\Delta t\right), \quad (10)$$

$$\mathbf{v}_k = \mathbf{v}_{k-1} + (\mathbf{R}_{k-1}(\mathbf{f}_{k-1} - \mathbf{b}_{f,k-1}) + \mathbf{g})\Delta t, \quad (11)$$

$$\mathbf{p}_k = \mathbf{p}_{k-1} + \mathbf{v}_k\Delta t. \quad (12)$$

where $\text{quat}(\cdot)$ represents the incremental quaternion constructed from the angular rate vector, \otimes denotes the quaternion product and \mathbf{g} is the gravity vector in the ENU navigation frame.

B. Velocity Corrections Using OBDII Module

To constrain the velocity drift from the INS mechanization, the OBDII interface provided an independent and reliable source of velocity information, which was incorporated into the EKF fusion. Since OBDII provides a scalar speed (v_{odometer}), representing the vehicle's longitudinal motion, this value must be projected into the ENU navigation frame to be compatible with the EKF state vector [41].

Using the estimated vehicle's azimuth (ψ) and pitch (θ) angles, the velocity components in the East (v_x), North (v_y), and Up (v_z) are derived as:

$$\begin{aligned} v_x &= \sin(\psi) \cos(\theta) v_{\text{odometer}}, \\ v_y &= \cos(\psi) \cos(\theta) v_{\text{odometer}}, \\ v_z &= \sin(\theta) v_{\text{odometer}}. \end{aligned} \quad (13)$$

C. Extended Kalman Filter (EKF) Design

The EKF is used to estimate the error state $\delta\mathbf{x}$, which represents the deviation of the nominal state from the true state.

The error state vector at epoch k is defined as:

$$\delta\mathbf{x}_k = [\delta\mathbf{p}_k^\top \quad \delta\mathbf{v}_k^\top \quad \delta\boldsymbol{\theta}_k^\top \quad \delta\mathbf{b}_{f,k}^\top \quad \delta\mathbf{b}_{w,k}^\top]^\top, \quad (14)$$

where $\delta\mathbf{p}_k$, $\delta\mathbf{v}_k$, and $\delta\boldsymbol{\theta}_k$ denote the position, velocity, and attitude errors, respectively. The terms $\delta\mathbf{b}_{f,k}$ and $\delta\mathbf{b}_{w,k}$ represent the accelerometer and gyroscope bias error. The nominal state \mathbf{x}_k is propagated by using the INS mechanization as detailed in Section VI-A.

The prediction step also comprises the computation the a priori covariance \mathbf{P}_k^- using the state transition matrix $\mathbf{F}_{x,k-1}$ and process noise covariance \mathbf{Q}_{k-1} :

$$\mathbf{P}_k^- = \mathbf{F}_{x,k-1} \mathbf{P}_{k-1}^+ \mathbf{F}_{x,k-1}^\top + \mathbf{Q}_{k-1}, \quad (15)$$

where

$$\mathbf{F}_{x,k-1} = \begin{bmatrix} \mathbf{I}_3 & \mathbf{I}_3\Delta t & \mathbf{0}_3 & \mathbf{0}_3 & \mathbf{0}_3 \\ \mathbf{0}_3 & \mathbf{I}_3 & -\mathbf{R}_{k-1}^+ \boldsymbol{\Omega}_{f,k-1} \Delta t & -\mathbf{R}_{k-1}^+ \Delta t & \mathbf{0}_3 \\ \mathbf{0}_3 & \mathbf{0}_3 & \exp(-\boldsymbol{\Omega}_{\omega,k-1} \Delta t)^\top & \mathbf{0}_3 & -\mathbf{I}_3 \Delta t \\ \mathbf{0}_3 & \mathbf{0}_3 & \mathbf{0}_3 & \mathbf{I}_3 & \mathbf{0}_3 \\ \mathbf{0}_3 & \mathbf{0}_3 & \mathbf{0}_3 & \mathbf{0}_3 & \mathbf{I}_3 \end{bmatrix},$$

$$\boldsymbol{\Omega}_{\omega,k-1} = \text{skew}(\boldsymbol{\omega}_{k-1} - \mathbf{b}_{\omega,k-1}^+),$$

$$\boldsymbol{\Omega}_{f,k-1} = \text{skew}(\mathbf{f}_{k-1} - \mathbf{b}_{f,k-1}^+),$$

and $\text{skew}(\cdot) \in \mathbb{R}^{3 \times 3}$ denotes the skew-symmetric matrix generated from a three-dimensional vector.

The process noise covariance \mathbf{Q}_{k-1} models IMU sensor noise and biases:

$$\mathbf{Q}_{k-1} = \text{diag}(\sigma_f^2 \Delta t^2 \mathbf{I}_3 \quad \sigma_w^2 \Delta t^2 \mathbf{I}_3 \quad \sigma_{b_f}^2 \Delta t \mathbf{I}_3 \quad \sigma_{b_w}^2 \Delta t \mathbf{I}_3). \quad (16)$$

where the values of these noise parameters were estimated using Allan Variance analysis, a widely used technique for IMU noise characterization [43].

The correction step updates the state using external measurements \mathbf{z}_k . In this system, two sources of corrections are applied independently: the speed correction from the odometer and the pose correction from VMR. The speed correction is applied first to constrain the velocity states, after which the corrected pose is passed to the VMR module. When an ICP-based registration measurement becomes available, it is used to further refine position and orientation estimates. For both corrections, the measurement model is:

$$\mathbf{z}_k = \mathbf{H}_k \delta\mathbf{x}_k + \boldsymbol{\eta}_k, \quad \boldsymbol{\eta}_k \sim \mathcal{N}(0, \mathbf{N}_k), \quad (17)$$

where $\mathbf{H}_k = [\mathbf{0}_3 \quad \mathbf{I}_3 \quad \mathbf{0}_3 \quad \mathbf{0}_3 \quad \mathbf{0}_3]$ for the speed correction, and

$$\mathbf{H}_k = \begin{bmatrix} \mathbf{I}_3 & \mathbf{0}_3 & \mathbf{0}_3 & \mathbf{0}_3 & \mathbf{0}_3 \\ \mathbf{0}_3 & \mathbf{0}_3 & \mathbf{I}_3 & \mathbf{0}_3 & \mathbf{0}_3 \end{bmatrix},$$

It should be noted that the measurement covariance, \mathbf{N}_k , was empirically derived from uncertainty analysis of the OBDII-based vehicle speed measurements and monocular depth estimation using offline test data.

Finally, the Kalman gain \mathbf{K}_k and update equations are executed as:

$$\mathbf{K}_k = \mathbf{P}_k^- \mathbf{H}_k^\top (\mathbf{H}_k \mathbf{P}_k^- \mathbf{H}_k^\top + \mathbf{N}_k)^{-1}. \quad (18)$$

$$\delta\mathbf{x}_k^+ = \delta\mathbf{x}_k^- + \mathbf{K}_k (\mathbf{z}_k - \mathbf{H}_k \delta\mathbf{x}_k^-), \quad (19)$$

$$\mathbf{P}_k^+ = (\mathbf{I} - \mathbf{K}_k \mathbf{H}_k) \mathbf{P}_k^- (\mathbf{I} - \mathbf{K}_k \mathbf{H}_k)^\top + \mathbf{K}_k \mathbf{N}_k \mathbf{K}_k^\top. \quad (20)$$

D. Dynamic Tuning

To improve robustness against measurement outliers, the measurement noise covariance \mathbf{N}_k is adaptively tuned based on the magnitude of the correction. The principle is to reduce certainty in measurements that deviate significantly from the current prior estimate.

The measurement covariance matrix \mathbf{N} is dynamically adjusted using a tuning vector $\boldsymbol{\lambda}$ defined as:

$$\boldsymbol{\lambda} = [\lambda_x \quad \lambda_y \quad \lambda_z \quad \lambda_\theta \quad \lambda_\phi \quad \lambda_\psi]^\top, \quad (21)$$

where λ_x , λ_y , and λ_z are the tuning factors for the East (x), North (y), and Up (z) directions, respectively, and λ_θ , λ_ϕ , and λ_ψ represent the tuning factors for pitch, roll, and azimuth, respectively.

The tuning factors for all components are computed as:

$$\lambda_i = \exp(\alpha \cdot |\Delta i|), \quad \text{for } i \in \{x, y, z, \theta, \phi, \psi\}, \quad (22)$$

where $\Delta i = i_{\text{new}} - i_{\text{est}}$ denotes the correction for each state component. The scaling hyperparameter α was empirically tuned to balance responsiveness with stability in the presence of measurement uncertainty.

The dynamically adjusted measurement covariance matrix $\mathbf{N}_{\text{dynamic}}$ is then computed as:

$$\mathbf{N}_{\text{dynamic}} = \mathbf{N}_{\text{static}} \cdot \text{diag}(\boldsymbol{\lambda}), \quad (23)$$

where $\mathbf{N}_{\text{static}}$ is the nominal measurement noise covariance matrix.

VII. EXPERIMENTAL SETUP AND MAPS DATASET

A. Sensor Configuration and Data Collection

The experimental evaluation was conducted using the navigation and instrumentation research lab (NavINST) platform [44], a research vehicle equipped with a tightly synchronized multi-sensor suite to support positioning research in both outdoor and indoor environments. A subset of the available sensors, highlighted in Fig. 6, was the focus of this study. All data were recorded using robot operating system (ROS), then temporally aligned to a common frequency of 10 Hz to reflect the relatively slow vehicle dynamics in all scenarios tested.

The primary sensors used include:

- A Luxonis OAK-1 W PoE monocular RGB camera operating at 30 Hz.
- An Xsens micro-electro-mechanical systems (MEMS)-grade IMU that provides inertial measurements at 100 Hz.
- An OBDII interface providing the vehicle's forward speed at 16 Hz.
- For outdoor experiments, ground truth was obtained at 50 Hz from a NovAtel PwrPak7-E1 system, comprising a high-end GNSS receiver, tactical-grade IMU (KVH-1750), with post-processed kinematic (PPK) corrections.
- For indoor experiments, where GNSS is unavailable, ground truth was obtained at 50 Hz from a multi-sensor system that integrates tactical-grade IMU, wheel odometry, and LiDAR registration with a pre-built high-accuracy 3-D map [41].

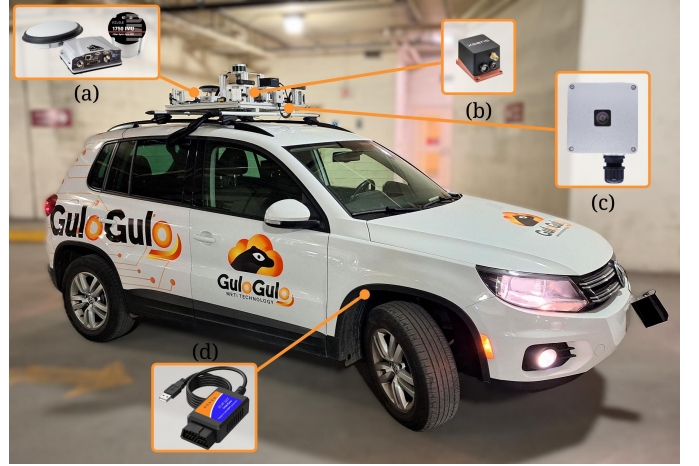


Fig. 6. NavINST Multi-Sensor Platform highlighting the primary sensors. (a) NovAtel PwrPak7-E1, (b) Xsens IMU, (c) Luxonis OAK-1 W PoE Camera, and (d) OBDII Module

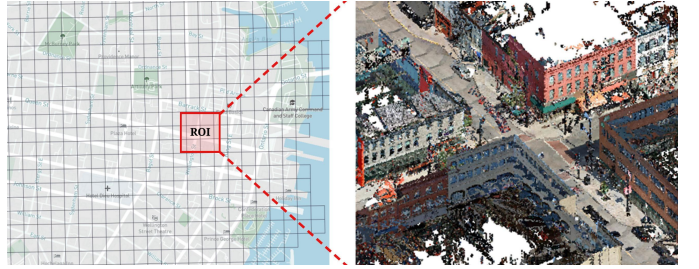


Fig. 7. A subset of the city of Kingston 3-D Maps.

B. 3-D Maps Dataset

The outdoor experiments utilize a high-accuracy 3-D map of downtown Kingston, Ontario, Canada. This map was generated through municipal mobile mapping efforts and includes dense street-level point cloud data from urban structures such as buildings, poles, and signage. The data consists of tens of thousands of `.las` files, each containing millions of 3-D georeferenced points. These 3-D files are organized within a geospatial database structured into spatial tiles with consistent geometry, where each tile references a corresponding 3-D `.las` file [45]. As shown in Fig. 7, specifying a spatial ROI retrieves relevant tiles, which are combined to construct a local

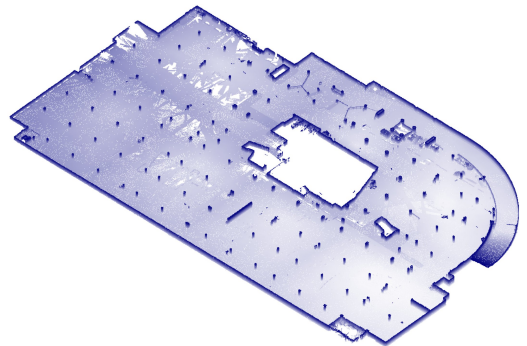


Fig. 8. 3-D map of the indoor parking garage.

3-D map. These maps serve as prior knowledge for accurate positioning in outdoor driving scenarios.

To validate the proposed method through indoor driving experiments, a 3-D map of an underground parking garage from the NavINST dataset [44]. The 3-D map, shown in Fig. 8, was created using a high-resolution stationary LiDAR scanner and refined through post-processing to remove irrelevant elements, such as stationary vehicles and pedestrians.

VIII. RESULTS AND DISCUSSION

The proposed method is evaluated in six representative segments: two indoors and four outdoors. These segments were carefully selected to cover a range of conditions, including varying feature density, structural complexity, and dynamic elements such as moving vehicles and pedestrians. For each segment, we compare three positioning approaches. The first is the OBMS EKF pipeline, which represents a baseline solution based solely on inertial mechanization corrected by forward speed measurements obtained from the vehicle odometer. This configuration does not incorporate vision-based updates or map registration.

The second method, referred to as vanilla VMR, implements visual map registration using raw monocular depth and image features, but excludes the enhancements introduced in this work, i.e., STOR, depth cropping, scale correction, point cloud filtering IV, distance-based aggregation V-C, and EKF dynamic tuning VI-D).

The third approach is the proposed VMR solution, which integrates all of the aforementioned enhancements to improve robustness and positioning accuracy across diverse environments. This comparison allows us to isolate the contributions and evaluate the overall effectiveness of the full pipeline under real-world constraints.

A. Indoors

The proposed VMR solution was evaluated on two challenging indoor trajectories recorded within a parking garage. Both segments reflect real-world structured environments characterized by poor lighting, low-texture surfaces, and frequent stop-and-go motions. The first segment (I1), spanning approximately 1.8 minutes (110 seconds), includes several turns, vehicle stops, and slow maneuvers with a peak speed of approximately 15 km/h. The second segment (I2) is notably longer, about 4.3 minutes (260 seconds), and includes tight loops and more aggressive maneuvers, with a maximum speed of approximately 18 km/h. This increased duration and complexity make segment I2 a more rigorous test of long-term drift resilience.

Fig. 9 illustrates a qualitative comparison between the three positioning solutions, where in both cases the proposed VMR system consistently outperforms the baseline OBMS and vanilla VMR approaches, providing a closer resemblance to the ground truth trajectory. These differences can be better demonstrated in the corresponding horizontal and heading error curves in Fig. 10.

A detailed quantitative comparison is summarized in TABLE II. In terms of horizontal accuracy, the OBMS solution

TABLE II
COMPARISON OF PERFORMANCE STATISTICS FOR INDOOR SEGMENTS 1 AND 2.

Metric		Segment I1			Segment I2		
		OBMS	Vanilla	Proposed	OBMS	Vanilla	Proposed
Position							
Horizontal	RMSE (m) ↓	4.23	1.74	0.70	6.31	20.45	0.91
	MaxAE (m) ↓	7.40	4.66	1.57	12.37	35.10	2.09
Vertical	RMSE (m) ↓	5.13	0.43	0.18	7.72	0.45	0.16
	MaxAE (m) ↓	8.05	0.68	0.37	10.11	0.77	0.42
Lane-level	(% < 1.5 m) ↑	17.23	57.16	99.18	3.99	10.96	89.73
Submeter-level	(% < 1 m) ↑	8.48	34.73	92.16	2.18	6.69	68.20
Attitude							
Pitch	RMSE (°) ↓	1.50	0.40	0.39	1.98	0.79	0.40
	MaxAE (°) ↓	3.26	1.49	1.05	4.42	3.20	1.05
Roll	RMSE (°) ↓	1.40	0.97	0.88	3.03	1.16	0.63
	MaxAE (°) ↓	3.07	2.89	1.95	7.52	3.52	1.79
Heading	RMSE (°) ↓	3.63	3.82	1.67	8.02	53.16	1.64
	MaxAE (°) ↓	6.31	9.39	4.44	13.64	167.72	4.64

accumulates drift over time due to its reliance on inertial propagation, resulting in substantial horizontal RMSE 4.23 m in segment I1 and 6.31 m in segment I2. Vanilla VMR provides modest improvements in segment I1 (1.74 m RMSE) but completely fails in segment I2 (20.45 m RMSE), where accumulated error exceeds the convergence threshold of the GICP algorithm, leading to failed registrations and continuous drift. In contrast, the proposed VMR maintains robust performance with horizontal RMSEs of 0.70 m in segment I1 and 0.91 m in segment I2, achieving approximately 84.5% improvement over OBMS and 77.7% over vanilla across both segments.

Similar improvements are also evident in the table with respect to other navigation states. For example, the vertical RMSE drops from 5.13 m (OBMS) and 0.43 m (vanilla) to 0.18 m with the proposed method, in segment I1. While in segment I2, vertical error dropped from 7.72 m for OBMS and 0.45 m for vanilla to 0.16 m. These results correspond to an average vertical RMSE improvement of 97.2% over OBMS and 61.3% over vanilla. Moreover, the heading RMSE remains consistent across both evaluations, 1.67° and 1.64°, showing about 66% improvement over OBMS and 76.6% over vanilla.

Finally, the proposed method achieves 99.18% of position errors within 1.5 m (lane-level accuracy) and 92.16% within 1 m (submeter-level) in segment I1. In the more challenging segment I2, it maintains 89.73% of errors within 1.5 m and 68.20% within 1 m. This corresponds to an average improvement of 74.9% over OBMS and 59.5% over vanilla in submeter-level positioning accuracy.

B. Outdoors

The proposed VMR solution was further evaluated across four outdoor segments varying in geometry and complexity, from straight urban roads to tight turns. Segment lengths ranged from 446 to 700 m, durations between 70 and 124 s, and speeds from 15 to 36 km/h. Despite environmental variation such as open parks, parking lots, dense buildings, and intersections, the proposed method demonstrated reliable positioning performance.

The performance of the proposed VMR solution across all outdoor segments is illustrated in Fig. 11, which shows

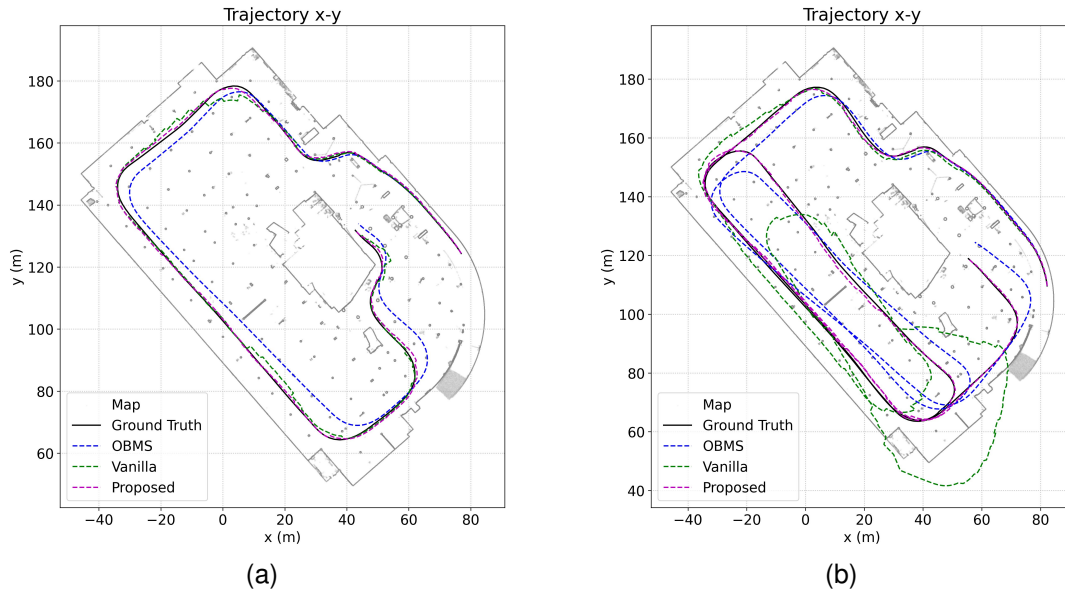


Fig. 9. Estimated trajectories of standalone OBMS, Vanilla VMR, and Proposed VMR in the indoor parking garage for (a) Segment I1 and (b) Segment I2.

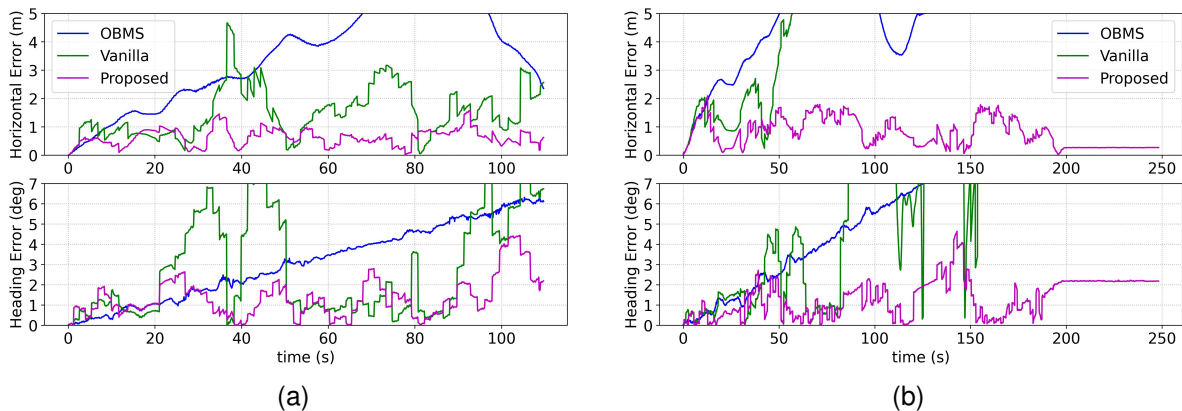


Fig. 10. Horizontal and heading errors of standalone OBMS, Vanilla VMR, and Proposed VMR in the indoor parking garage for (a) Segment I1 and (b) Segment I2.

TABLE III
COMPARISON OF PERFORMANCE STATISTICS FOR OUTDOOR SEGMENTS 1–4.

Metric		Segment O1			Segment O2			Segment O3			Segment O4		
		OBMS	Vanilla	Proposed									
Position													
Horizontal	RMSE (m) ↓	41.00	3.39	0.78	21.03	6.15	1.03	16.24	2.67	1.25	21.69	1.82	1.29
	MaxAE (m) ↓	74.68	9.51	2.02	36.51	26.79	2.21	31.54	6.56	3.46	46.53	3.67	3.35
Vertical	RMSE (m) ↓	39.08	0.94	0.12	17.40	0.97	0.23	11.70	1.02	0.26	15.93	1.03	0.11
	MaxAE (m) ↓	72.47	1.47	0.30	30.94	1.63	0.48	23.00	1.53	0.52	37.55	1.37	0.30
Lane-level	% < 1.5 m ↑	7.43	41.20	95.20	10.52	26.45	85.91	20.57	43.54	76.00	12.14	51.17	72.43
Submeter-level	% < 1 m ↑	5.84	27.84	81.68	5.62	11.64	62.73	17.00	30.15	60.15	8.29	28.83	57.86
Attitude													
Pitch	RMSE (°) ↓	8.65	0.78	0.24	5.90	0.90	0.37	3.07	0.72	0.48	4.54	0.40	0.30
	MaxAE (°) ↓	14.66	2.69	1.00	10.22	3.38	1.02	5.62	2.50	2.34	8.68	1.52	1.32
Roll	RMSE (°) ↓	0.67	1.30	0.64	3.81	2.09	1.25	2.62	0.93	0.68	1.45	1.40	0.76
	MaxAE (°) ↓	1.22	3.57	2.09	10.19	5.65	3.78	5.06	2.42	2.04	2.66	4.40	1.93
Heading	RMSE (°) ↓	7.06	1.85	0.69	6.42	8.67	1.11	4.19	1.44	0.98	3.67	1.66	1.18
	MaxAE (°) ↓	12.24	5.01	2.18	11.55	38.01	3.25	7.32	4.57	2.49	6.41	6.33	3.45

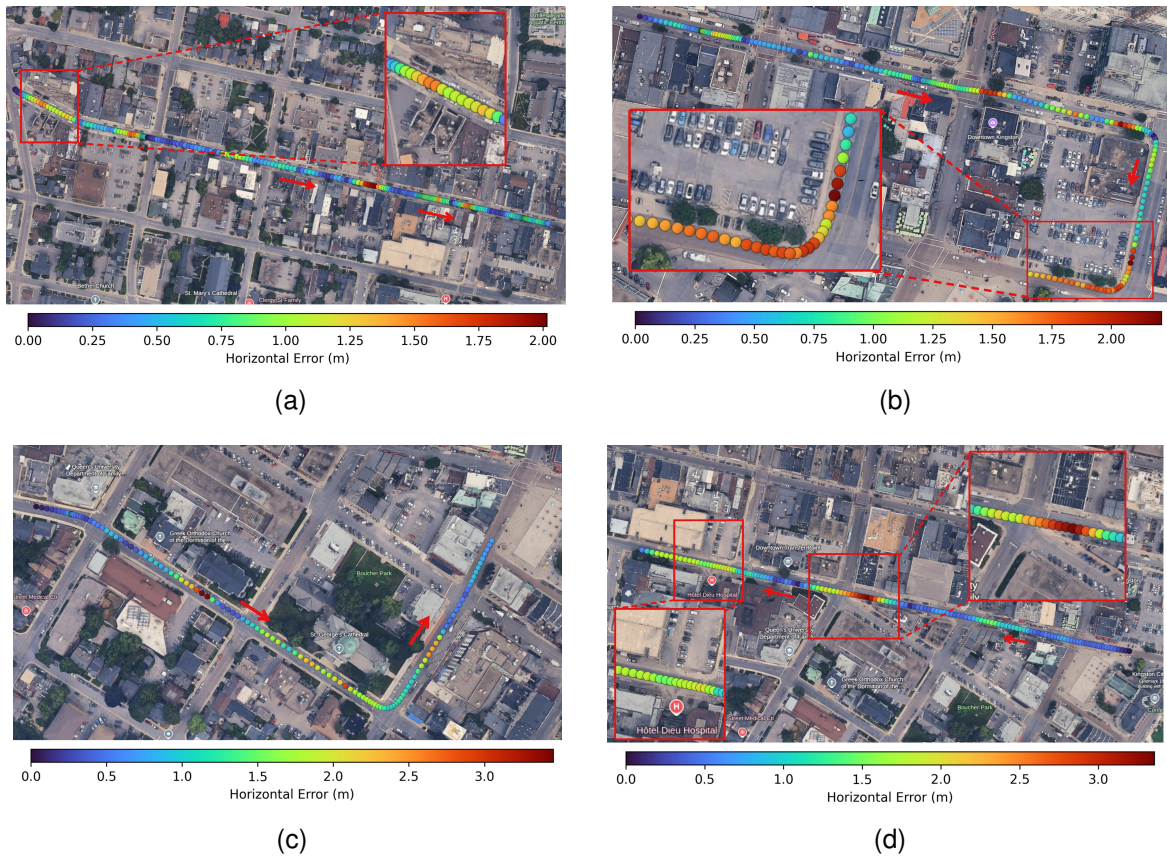


Fig. 11. Proposed VMR trajectory color-coded by horizontal positioning error for (a) Segment O1, (b) Segment O2, (c) Segment O3, and (d) Segment O4.

Google Earth plots of the estimated trajectories color-coded by horizontal positioning error. The trajectory plots demonstrate a consistent, drift-free performance across varying outdoor conditions. Fig. 12 further demonstrates the pose estimation performance across the same segments, highlighting the benefits of the proposed method in terms of horizontal position and heading errors compared to the examined baselines.

TABLE III provides the quantitative analysis between the different segments and positioning solutions. The OBMS baseline exhibited significant drift, with horizontal RMSEs ranging from 16.24 m to 41.00 m. Vanilla VMR improved this baseline by approximately 85–92%, but continued to suffer from poor convergence and failures, especially in feature-sparse areas. In contrast, the proposed method further reduced horizontal RMSE compared to vanilla VMR, resulting in final RMSEs between 0.78 m and 1.29 m. The proposed method achieves an average of 88% reduction over OBMS and 74% over vanilla VMR in horizontal RMSE.

Submeter-level positioning varied based on scene geometry and feature availability. Segment O1 achieved the highest precision, with 81.68% of positioning errors within 1 m and 95.20% within 1.5 m. Segment O2, shown in Fig. 11b and involved sharp turns and open structures like parking lots, achieved 62.73% submeter accuracy and 85.91% within 1.5 m. Segments O3 and O4 performed similarly with 60.15% and 57.86% of positions within 1 m, respectively. These localized fluctuations in performance can be observed in the correspond-

ing horizontal error plots in Fig. 12.

Heading estimation trends followed a similar pattern to horizontal errors. As shown in the error plots, both OBMS and vanilla VMR suffered from increasing drift, with heading RMSEs ranging from 3.67° to 8.67° . The proposed method, however, consistently reduced heading RMSE by approximately 70–90% relative to both baselines. Averaged across all segments, the heading RMSE improvement was around 80% over OBMS and 75% over vanilla VMR, maintaining heading errors below 1.3° in all cases. Segment O1 achieved the best result (0.69°) due to its linear geometry and stable features, while segment O4 had the highest heading RMSE (1.18°) as a result of visual aliasing and weak structural context near intersections.

Scene complexity varied across segments, causing localized increases in error for all methods. In Segment O1, errors rose at the beginning due to an open area with few features and near intersections where abrupt depth changes occurred (Fig. 11a, Fig. 12a). Segment O2 showed error spikes primarily after the second 90° turn near open parking garages and parks across from it (Fig. 11b, Fig. 12b). Segment O3's errors fluctuated along the route, notably when passing next to a small parking lot, otherwise it showed consistent errors (Fig. 11c, Fig. 12c). Segment O4 experienced increased errors at a central wide intersection with distant buildings and near a parking garage and hospital entrance (Fig. 11d, Fig. 12d). Despite these error increases, the robust fusion filter within the

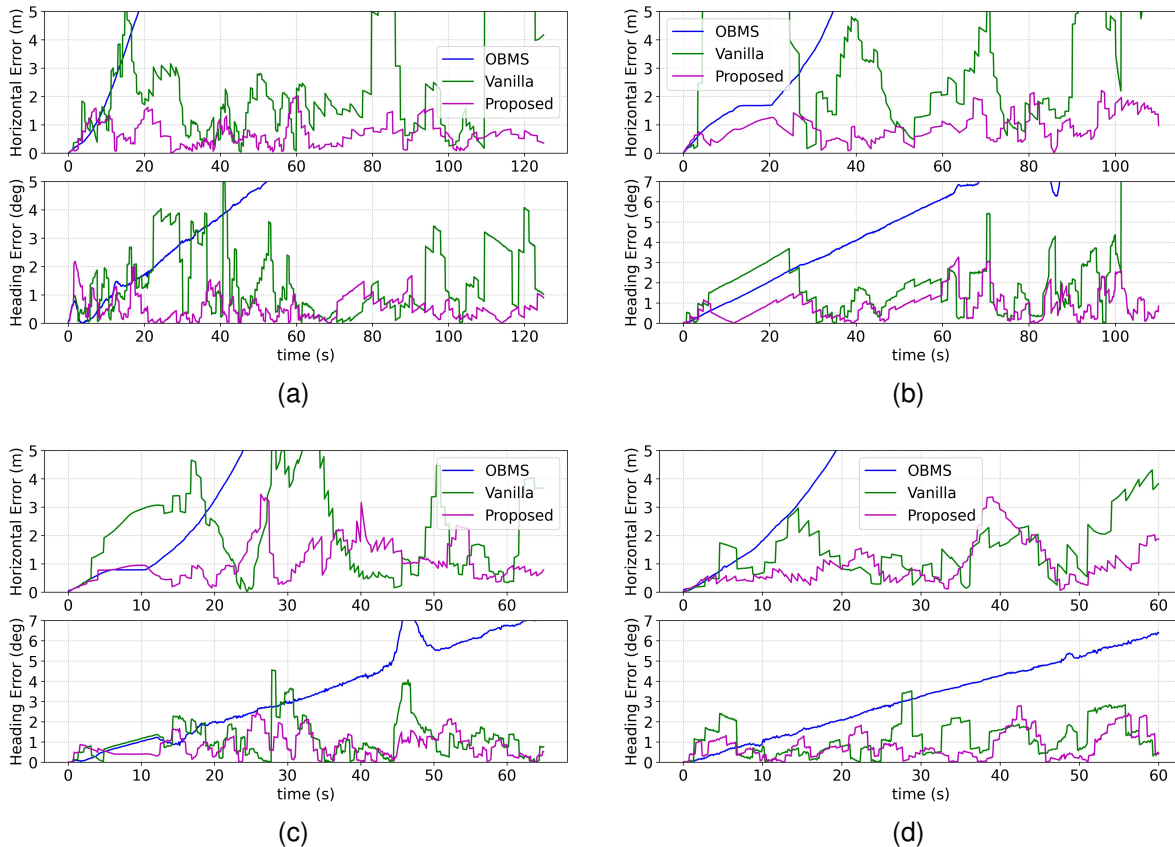


Fig. 12. Horizontal and heading errors for standalone OBMS, Vanilla VMR, and Proposed VMR in (a) Segment O1, (b) Segment O2, (c) Segment O3, and (d) Segment O4.

proposed system effectively leveraged INS, speed corrections, and dynamic tuning to recover positioning accuracy, reduce drift, and maintain submeter-level precision throughout the trajectories.

IX. CONCLUSION

This paper presented a robust, scalable positioning solution for autonomous vehicles operating in GNSS-challenged environments. Leveraging recent advances in monocular depth estimation, semantic filtering, and 3-D map alignment, the proposed system delivers consistent sub-meter accuracy using only low-cost sensors. Unlike traditional LiDAR systems, this approach is lightweight, cost-effective, and deployable in existing vehicle sensor architectures.

Future directions include extending to multi-camera systems for wider field-of-view coverage and evaluating cross-city generalization under diverse lighting and seasonal conditions. This study lays the foundation for the practical deployment of vision-driven navigation systems in real-world autonomous platforms.

ACKNOWLEDGMENTS

The authors acknowledge the Centre for Advanced Computing (CAC), Queen’s University, and Micro Engineering Tech Inc. (METI) for providing the 3-D maps used in this research.

REFERENCES

- [1] L. Chen, Y. Li, L. Li, S. Qi, J. Zhou, Y. Tang, J. Yang, and J. Xin, “High-precision positioning, perception and safe navigation for automated heavy-duty mining trucks,” *IEEE Transactions on Intelligent Vehicles*, vol. 9, no. 4, pp. 4644–4656, 2024.
- [2] Y. Zhang, F. Zhu, Q. Cai, J. Lv, Z. Xu, X. Chen, and X. Zhang, “Towards more precise and robust positioning in urban environments through an enhanced fgo-based gnss rtk framework,” *IEEE Transactions on Intelligent Vehicles*, pp. 1–15, 2024.
- [3] P. Puricer and P. Kovar, “Technical limitations of gnss receivers in indoor positioning,” in *2007 17th International Conference Radioelektronika*, 2007, pp. 1–5.
- [4] J. Jo, J. Seok, S. Kim, Y. Kim, N. Kim, M. Jeong, and K. Jo, “Real-time road surface lidar slam based on dead-reckoning assisted registration,” *IEEE Transactions on Intelligent Vehicles*, pp. 1–12, 2024.
- [5] M. Petovello, M. Cannon, and G. Lachapelle, “Benefits of using a tactical-grade imu for high-accuracy positioning,” *Navigation*, vol. 51, no. 1, pp. 1–12, 2004.
- [6] A. Pidurkar, R. Sadakale, and A. Prakash, “Monocular camera based computer vision system for cost effective autonomous vehicle,” in *2019 10th International Conference on Computing, Communication and Networking Technologies (ICCCNT)*, 2019, pp. 1–5.
- [7] S. Choi, J. Park, and W. Yu, “Resolving scale ambiguity for monocular visual odometry,” in *2013 10th International Conference on Ubiquitous Robots and Ambient Intelligence (URAI)*, 2013, pp. 604–608.
- [8] M. Hu, W. Yin, C. Zhang, Z. Cai, X. Long, H. Chen, K. Wang, G. Yu, C. Shen, and S. Shen, “Metric3d v2: A versatile monocular geometric foundation model for zero-shot metric depth and surface normal estimation,” *IEEE Transactions on Pattern Analysis and Machine Intelligence*, 2024.
- [9] A. Chalvatzaras, I. Pratikakis, and A. A. Amanatiadis, “A survey on map-based localization techniques for autonomous vehicles,” *IEEE Transactions on Intelligent Vehicles*, vol. 8, no. 2, pp. 1574–1596, 2023.

- [10] G. Mao, K. Wang, Z. Zhang, T. Fu, and X. Qu, "Iot-based vehicle localization in gnss-denied environments," in *GLOBECOM 2024 - 2024 IEEE Global Communications Conference*, 2024, pp. 265–270.
- [11] O. Elmaghraby, P. R. M. Araujo, S. I. K. Abdelaziz, and A. Noureldin, "Comparative study of traditional and deep learning feature detectors and matchers for land vehicle monocular visual odometry," in *2025 IEEE International systems Conference (SysCon)*, 2025, pp. 1–8.
- [12] G. Bresson, Z. Alsayed, L. Yu, and S. Glaser, "Simultaneous localization and mapping: A survey of current trends in autonomous driving," *IEEE Transactions on Intelligent Vehicles*, vol. 2, no. 3, pp. 194–220, 2017.
- [13] K. Yousif, A. Bab-Hadiashar, and R. Hoseinnezhad, "An overview to visual odometry and visual slam: Applications to mobile robotics," *Intelligent Industrial Systems*, vol. 1, no. 4, pp. 289–311, 2015. [Online]. Available: <https://doi.org/10.1007/s40903-015-0032-7>
- [14] T. Qin, P. Li, and S. Shen, "Vins-mono: A robust and versatile monocular visual-inertial state estimator," *IEEE Transactions on Robotics*, vol. 34, no. 4, pp. 1004–1020, 2018.
- [15] N. Reginald, O. Al-Buraiki, T. Choopojcharoen, B. Fidan, and E. Hashemi, "Visual-inertial-wheel odometry with slip compensation and dynamic feature elimination," *Sensors*, vol. 25, no. 5, p. 1537, 2025.
- [16] T.-K. Jung and G.-I. Jee, "Va-loam: Visual assist lidar odometry and mapping for accurate autonomous navigation," *Sensors*, vol. 24, no. 12, p. 3831, 2024.
- [17] W.-z. Peng, Y.-h. Ao, J.-h. He, and P.-f. Wang, "Vehicle odometry with camera-lidar-imu information fusion and factor-graph optimization," *Journal of Intelligent & Robotic Systems*, vol. 101, 04 2021.
- [18] L. Lou, Y. Li, Q. Zhang, and H. Wei, "SLAM and 3D Semantic Reconstruction Based on the Fusion of Lidar and Monocular Vision," *Sensors*, vol. 23, no. 3, p. 1502, Jan 2023.
- [19] D. Wofk, F. Ma, T.-J. Yang, S. Karaman, and V. Sze, "Fastdepth: Fast monocular depth estimation on embedded systems," in *2019 International Conference on Robotics and Automation (ICRA)*, 2019, pp. 6101–6108.
- [20] C. Godard, O. M. Aodha, M. Firman, and G. Brostow, "Digging into self-supervised monocular depth estimation," in *2019 IEEE/CVF International Conference on Computer Vision (ICCV)*, 2019, pp. 3827–3837.
- [21] G. Elazab, T. Gräber, M. Unterreiner, and O. Hellwich, "Monopp: Metric-scaled self-supervised monocular depth estimation by planar-parallax geometry in automotive applications," in *2025 IEEE/CVF Winter Conference on Applications of Computer Vision (WACV)*, 2025, pp. 2777–2787.
- [22] L. Yang, B. Kang, Z. Huang, Z. Zhao, X. Xu, J. Feng, and H. Zhao, "Depth anything v2," <https://arxiv.org/abs/2406.09414>, 2024, arXiv:2406.09414.
- [23] S. Bhat, R. Birkl, D. Wofk, P. Wonka, and M. Mueller, "Zoedepth: Zero-shot transfer by combining relative and metric depth," 02 2023.
- [24] W. Yin, C. Zhang, H. Chen, Z. Cai, G. Yu, K. Wang, X. Chen, and C. Shen, "Metric3d: Towards zero-shot metric 3d prediction from a single image," in *Proceedings of the IEEE/CVF International Conference on Computer Vision*, 2023, pp. 9043–9053.
- [25] J. M. Kang, T. S. Yoon, E. Kim, and J. B. Park, "Lane-level map-matching method for vehicle localization using gps and camera on a high-definition map," *Sensors*, vol. 20, no. 8, p. 2166, 2020. [Online]. Available: <https://doi.org/10.3390/s20082166>
- [26] A. Chalvatzaras, I. Pratikakis, and A. A. Amanatiadis, "A survey on map-based localization techniques for autonomous vehicles," *IEEE Transactions on Intelligent Vehicles*, vol. 8, no. 2, pp. 1574–1596, 2023.
- [27] J. Jung, J. Yoon, H. Lee, H. Darweesh, and W. Sung, "Tutorial on high-definition map generation for automated driving in urban environments," *Sensors*, vol. 22, p. 7056, 09 2022.
- [28] C. Lopes, R. Maffei, and M. Kolberg, "Monocular depth estimation applied to global localization over 2d floor plans using free space density," *Journal of Intelligent & Robotic Systems*, vol. 111, no. 1, p. 4, 2024. [Online]. Available: <https://doi.org/10.1007/s10846-024-02131-1>
- [29] E. Dawson, "Integrated remote sensing and map registration system for high-precision positioning in covered parking garages," in *Proceedings of the 36th International Technical Meeting of the Satellite Division of The Institute of Navigation (ION GNSS+)*, Denver, Colorado, September 2023, pp. 1633–1643.
- [30] H. Yu, W. Zhen, W. Yang, J. Zhang, and S. Scherer, "Monocular camera localization in prior lidar maps with 2d-3d line correspondences," in *2020 IEEE/RSJ International Conference on Intelligent Robots and Systems (IROS)*, 2020, pp. 4588–4594.
- [31] L. Zhao, Z. Liu, Q. Yin, L. Yang, and M. Guo, "Towards robust visual localization using multi-view images and hd vector map," in *2024 IEEE International Conference on Image Processing (ICIP)*, 2024, pp. 814–820.
- [32] K. Chen, H. Yu, W. Yang, L. Yu, S. Scherer, and G.-S. Xia, "I2d-loc: Camera localization via image to lidar depth flow," *ISPRS Journal of Photogrammetry and Remote Sensing*, vol. 194, pp. 209–221, 12 2022.
- [33] H. Wang, Y. Liu, B. Wang, Y. Sun, Z. Dong, W. Wang, and B. Yang, "Freereg: Image-to-point cloud registration leveraging pre-trained diffusion models and monocular depth estimators," *arXiv preprint arXiv:2310.03420*, 2023.
- [34] D. Singh and B. Singh, "Investigating the impact of data normalization on classification performance," *Applied Soft Computing*, vol. 97, p. 105524, 2020. [Online]. Available: <https://www.sciencedirect.com/science/article/pii/S1568494619302947>
- [35] H. Peng, Z. Zhao, and L. Wang, "A review of dynamic object filtering in slam based on 3d lidar," *Sensors*, vol. 24, no. 2, 2024. [Online]. Available: <https://www.mdpi.com/1424-8220/24/2/645>
- [36] Y. Wu, A. Kirillov, F. Massa, W.-Y. Lo, and R. Girshick, "Detectron2," <https://github.com/facebookresearch/detectron2>, 2019.
- [37] J. Chawla, N. Thakurdesai, A. Godase, M. A. Reza, D. J. Crandall, and S.-H. Jung, "Error diagnosis of deep monocular depth estimation models," *2021 IEEE/RSJ International Conference on Intelligent Robots and Systems (IROS)*, pp. 5344–5649, 2021. [Online]. Available: <https://api.semanticscholar.org/CorpusID:237455620>
- [38] A. Masoumian, D. G. F. Marei, S. Abdulwahab, J. Cristiano, D. Puig, and H. A. Rashwan, "Absolute distance prediction based on deep learning object detection and monocular depth estimation models," in *International Conference of the Catalan Association for Artificial Intelligence*, 2021. [Online]. Available: <https://api.semanticscholar.org/CorpusID:240420037>
- [39] P. J. Besl and N. D. McKay, "A method for registration of 3-d shapes," *IEEE Transactions on Pattern Analysis and Machine Intelligence*, vol. 14, no. 2, pp. 239–256, 1992.
- [40] A. V. Segal, D. Hähnel, and S. Thrun, "Generalized-icp," in *Robotics: Science and Systems*, 2009. [Online]. Available: <https://api.semanticscholar.org/CorpusID:231748613>
- [41] E. Mounier, M. Elhabiby, M. Korenberg, and A. Noureldin, "Lidar-based multisensor fusion with 3-d digital maps for high-precision positioning," *IEEE Internet of Things Journal*, vol. 12, no. 6, pp. 7209–7224, 2025.
- [42] P. R. M. de Araujo, E. Dawson, M. Elhabiby, S. Givigi, and A. Noureldin, "Evaluation of invariant extended kalman filters applied to multi-sensor land vehicle navigation in GNSS challenging environments," in *Proceedings of the 35th International Technical Meeting of the Satellite Division of The Institute of Navigation (ION GNSS+ 2022)*, Denver, Colorado, Sep. 2022, pp. 1631–1649. [Online]. Available: <https://doi.org/10.33012/2022.1847>
- [43] N. El-Sheimy, H. Hou, and X. Niu, "Analysis and modeling of inertial sensors using allan variance," *Instrumentation and Measurement, IEEE Transactions on*, vol. 57, pp. 140 – 149, 02 2008.
- [44] P. R. M. de Araujo, E. Mounier, Q. Bader, E. Dawson, S. I. K. Abdelaziz, A. Zekry, M. Elhabiby, and A. Noureldin, "The navinst dataset for multi-sensor autonomous navigation," *IEEE Access*, pp. 1–1, 2025.
- [45] E. Mounier, S. K. Abdelaziz, P. R. M. de Araujo, S. Taghavikish, M. Elhabiby, and A. Noureldin, "Utilizing lidar registration on 3d high accuracy digital maps for robust positioning in gnss challenging environments," in *Proceedings of the 35th International Technical Meeting of the Satellite Division of The Institute of Navigation (ION GNSS+ 2022)*, 2022, pp. 1366–1376.



Ola Elmaghraby received the B.Sc. degree in Electrical Engineering from Cairo University, Egypt, in 2023. She received her M.Sc. degree in Electrical and Computer Engineering at Queen's University, Canada, in 2025. Ola is also a member of the Navigation and Instrumentation Research Laboratory (NavINST) at the Royal Military College of Canada (RMCC). Her research interests include positioning for autonomous vehicles using computer vision integrated with inertial and odometer sensors.



Eslam Mounier (M'25) received the B.Sc. and M.Sc. degrees in computer and systems engineering (CSE) from Ain Shams University, Cairo, Egypt, in 2014 and 2020, and the Ph.D. degree in electrical and computer engineering (ECE) from Queen's University, Kingston, ON, Canada in 2025. He is currently a Postdoctoral Researcher with the School of Computing, Queen's University, Kingston, ON, Canada, and also with the Navigation and Instrumentation Research Laboratory (NavINST), Royal Military College of Canada (RMCC), Kingston.

His primary research interests include multisensor navigation systems for autonomous vehicles, advanced machine perception and computer vision techniques, and machine learning and deep learning applications.



Paulo Ricardo Marques de Araujo (M'24) received a Ph.D. in Electrical and Computer Engineering from Queen's University, Kingston, ON, Canada. His broader research interests include autonomous systems, robotics, machine learning, and digital manufacturing.



Aboelmagd Noureldin (SM'08) is a Professor and Canada Research Chair (CRC) at the Department of Electrical and Computer Engineering, Royal Military College of Canada (RMC), with Cross-Appointment at both the School of Computing and the Department of Electrical and Computer Engineering, Queen's University. He is also the founding director of the Navigation and Instrumentation (NavINST) research group at RMC, a unique world-class research facility in GNSS, wireless positioning, inertial navigation, remote sensing, and multisensory

fusion for navigation and guidance. Dr. Noureldin holds a Ph.D. in Electrical and Computer Engineering (2002) from The University of Calgary, Alberta, Canada. In addition, he has a B.Sc. in Electrical Engineering (1993) and an M.Sc. degree in Engineering Physics (1997), both from Cairo University, Egypt. Dr. Noureldin is a Senior member of the IEEE and a professional member of the Institute of Navigation (ION). He published two books, four book chapters, and over 350 papers in academic journals, conferences, and workshop proceedings, for which he received several awards. Dr. Noureldin's research led to 13 patents and several technologies licensed to the industry in position, location, and navigation systems.